Measurement of Elliptic Flow in p+Au Collisions at $\sqrt{s_{_{NN}}}=$ 200 GeV using the PHENIX Detector at RHIC

by

Theodore Koblesky

B.S., University of Illinois, 2011

A thesis submitted to the

Faculty of the Graduate School of the

University of Colorado in partial fulfillment

of the requirements for the degree of

Doctor of Philosophy

Department of Physics

2017

This thesis entitled:
Measurement of Elliptic Flow in p+Au Collisions at $\sqrt{s_{NN}}$= 200 GeV using the PHENIX Detector at RHIC
written by Theodore Koblesky
has been approved for the Department of Physics

Professor James Nagle

Prof. Standin

Ms. Standin

Date

The final copy of this thesis has been examined by the signatories, and we find that both the content and the form meet acceptable presentation standards of scholarly work in the above mentioned discipline.

Koblesky, Theodore (Ph.D., High Energy Nuclear Physics)

Measurement of Elliptic Flow in p+Au Collisions at $\sqrt{s_{NN}}$= 200 GeV using the PHENIX Detector at RHIC

Thesis directed by Professor James Nagle

Quark Gluon Plasma (QGP), a hot and dense state of matter in which quarks are not confined inside hadrons, is thought to be the same as the universe approximately one microsecond after the big bang. In Au+Au collisions at $\sqrt{s_{NN}}$= 200 GeV at the Relativistic Heavy Ion Collider (RHIC) and Pb+Pb collisions at $\sqrt{s_{NN}}$= 2.76 TeV at the Large Hadron Collider (LHC), QGP has been discovered to have unique properties, such as its opacity to color charges and the fact it behaves like a near-perfect fluid. Collective behavior in the form of a substantial elliptical azimuthal anisotropy (v_2) in the momentum distribution of final state particles has been observed, indicating a strongly-coupled, hydrodynamically flowing medium. Recently, features of collectivity have been detected in high-multiplicity, small collision systems thought to be too small to produce QGP, such as ^{3}He+Au and d+Au at $\sqrt{s_{NN}}$= 200 GeV, $p + Pb$ at $\sqrt{s_{NN}}$= 5 TeV, and even in $p + p$ at $\sqrt{s}$ = 13 TeV events. In order to constrain models seeking to describe this phenomena, collision systems with distinct initial collision geometries were run at RHIC: ^{3}He+Au for triangular geometry, d+Au for elliptical geometry, and p+Au for circular geometry. This thesis is the completion of that set of three measurements, by measuring v_2 in the p+Au. Comparisons of v_2 in the three collision systems and various theoretical models are made.

Dedication

Acknowledgements

People

Contents

Chapter

Tables

Table

Figures

Figure

Chapter 1

Analysis

This chapter is an extensive discussion of the information and data analysis techniques used to extract the measurement. First we will describe about the building blocks of the v_2 measurement, then we will examine the event plane analysis techniques, and the systematic errors.

1.1 The Building Blocks of the Measurement

Prior to any analysis, the raw data collected by various PHENIX subsystems must be reconstructed into well-defined software objects encapsulating the physical properties of the particles that traversed the detector. Although we have already discussed the subsystems used in this analysis in Chapter 3, this section provides in-depth information on central arm tracks, FVTX clusters, and BBC photomultiplier tubes (PMTs), and the physics variables they contain. Figure 1.1 displays the coordinate system for PHENIX and the particle parameters that are in relation to it.

1.1.1 Central Arm Tracks

Central arm (CA) tracks are the representation of charged particles emitted from the heavy ion collision, which are detected by detectors in the PHENIX central arms. There are two central arms, each one covering an acceptance of $\eta < |0.35|$ and $\frac{\pi}{2}$ in pseudorapidity and azimuth, respectively. The relevant detectors for this analysis include the Drift Chamber (DC), the Pad Chambers (PC) and the Ring Imaging Cerenkov (RICH) detector. As previously discussed, the drift chamber provides momentum information; the pad chambers provide track quality metrics; and the RICH

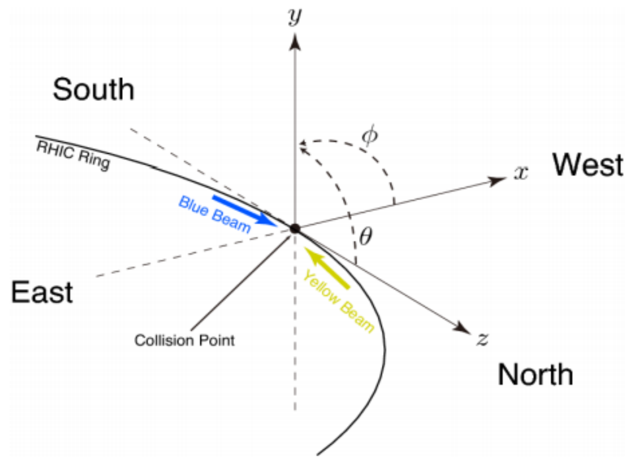

Figure 1.1: Reference coordinate system for the PHENIX detector. The origin is set at the collision point, around which the detector is centered. The beam runs parallel to the (longitudinal) $z-$axis, where the direction of positive z is defined as **north**. The **east** and **west** directions are defined as perpendicular to the longitudinal direction, where the direction of positive x is defined as west.

provides electron identification.

The main physical parameter of CA tracks is the momentum vector $\vec{p} = (p_x, p_y, p_z)$ of the particles, defined at the collision vertex. This analysis uses tracks with momentum $0.02 < |p_T| < 3.5$ GeV/c, where the momentum resolution is good, as shown in Fig. 1.6. The azimuthal angle and pseudorapidity of the track are calculated from the components of its momentum vector, as follows:

$$\phi = \arctan(\frac{p_y}{p_x}), \tag{1.1}$$

$$\eta = ArcSinH(\frac{p_z}{p_T}). \tag{1.2}$$

Table 1.1: Quality categorization of CA tracks, as a function of PC1 and DC wire hits. The quality parameters used in this analysis are 31 and 63.

Quality	PC1 found	PC1 unique	UV found	UV unique
17,18,19	1	0	0	0
21,22,23	1	0	1	0
29,30,31	1	0	1	1
49,50,51	1	1	1	0
61,62,63	1	1	1	1

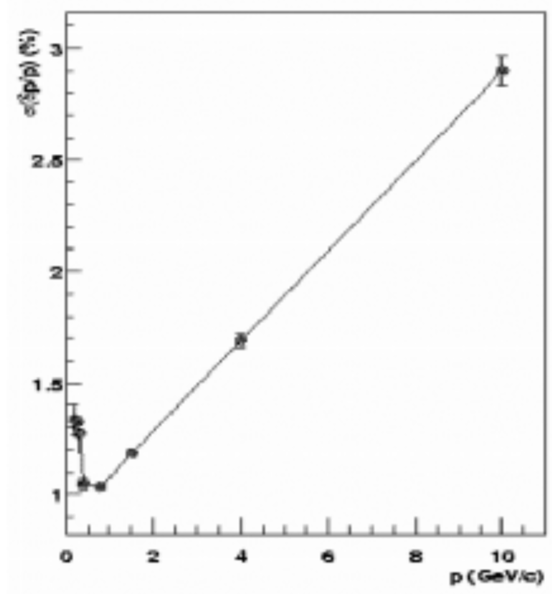

Figure 1.2: Momentum resolution σ_p/p as a function of the reconstructed track momentum, p for simulated single-particle events[2].

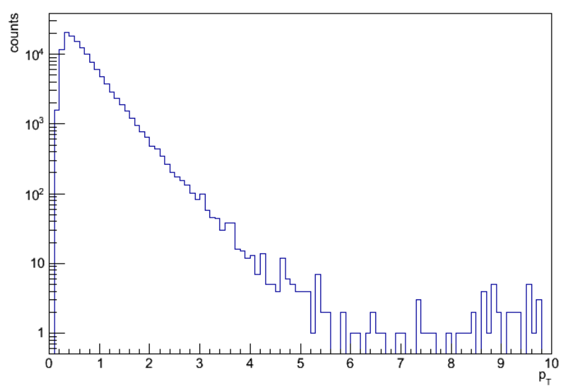

Figure 1.3: Transverse momentum p_T distribution of CA tracks in p+Auevents at $\sqrt{s_{NN}}$= 200 GeV. High p_T tracks observed correspond to unsubtracted background.

Table 1.2: Quality categorization of CA tracks, as a function of DC wire momentum information. The quality parameters used in this analysis are 31 and 63.

Quality	X1 used	X2 used
17,21,29,49,61	1	0
18,22,30,50,62	0	1
19,23,31,51,63	1	1

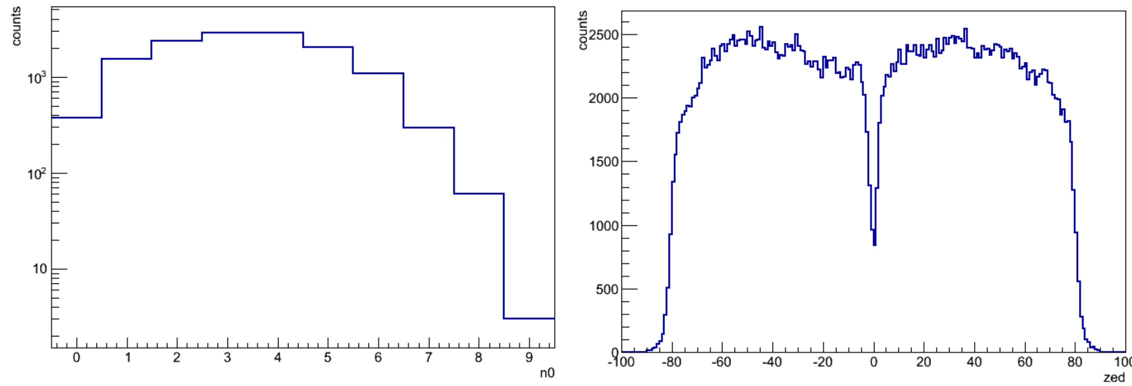

Figure 1.4: The distribution of (left) $n0$, i.e., the number of PMTs fired in the RICH, and (right) zed, i.e., the longitudinal position of tracks in the DC, for CA tracks in 0-5% central p+Auevents at $\sqrt{s_{NN}}$= 200 GeV. The structure observed in the zed distribution corresponds to a gap in the detector acceptance.

In addition to momentum, CA tracks provide a number of other parameters that can be used to ensure the quality of tracks and isolate a sample corresponding to charged hadrons. These include zed in the DC, dϕ and dz in the PC, $n0$ in the RICH, and the general track quality calculated from DC and PC information. These variables are defined as follows:

- The zed variable corresponds to the longitudinal position of the track in the DC, as shown in Fig. 1.4
- The dphi and dz variables quantify the distance between a track projection and its associated hits in the PC. In order to make standard cuts on these variables, their distribution must be calibrated to a standard Gaussian in a procedure known as sigmalization, described in subsection 1.1.1.1
- The $n0$ variable, used for electron identification, corresponds to the the number of PMTs fired in the RICH that match the DC track projection, as shown in Fig. 1.4

Table 1.3: Central Arm Track Cuts.

variable	cuts	units
p	$0.02 < p < 10.0$	GeV/c
zed	$\lvert zed \rvert$ <75	cm
PC3 dϕ	$\lvert d\phi \rvert$ <2.0	radians $\times 10^9$
PC3 dz	$\lvert dz \rvert$ <2.0	cm
n0	n0<=0	count
quality	63 or 31	N/A

1.1.1.1 Sigmalization of PC Variables

The goal of PC variables dz and dϕ is to provide criteria to determine if the ϕ orientation and z-direction of the track match between the third layer of the PC and the DC. The sigmalization is done in the minimum bias sample and is valid for all other centrality selections. We did the sigmalization procedure for tracks in different transverse momentum bins, separately in the east and west arms, and for positive and negative particles. The dϕ and dz distributions were fitted with a double-Gaussian function and then the parameters were smoothed as a function of p_T . Fig. 1.1.1.1 a) shows a fit to the sigmalized dϕ distribution, and Fig. 1.1.1.1 b) shows a fit to the sigmalized dz distribution for tracks with $1.0 < p_T < 1.1$ (GeV/c) in both the west and east arms as well as both positively and negatively charged particles. Then we fit the signal Gaussian mean and sigma by some polynomial functions. Once these variables had been sigmalized, we selected only the tracks within a 2σ cut.

1.1.2 FVTX Clusters

The FVTX consists of four silicon layers in the north and south directions, covering an acceptance of $1 < |\eta| < 3$ and spanning the full azimuth. FVTX clusters correspond to the spatial location where charged particles hit one of the silicon layers. Each cluster is expected to correspond to a single charged particle in the case of p+Aucollisions, because of the low multiplicity relative to Au+Au collisions. These clusters have a spatial resolution in x and y of 50 μm, and have an RMS along the z-direction that corresponds to the width of an FVTX layer, of $\frac{200}{\sqrt{12}}$ μm [10]. Due to

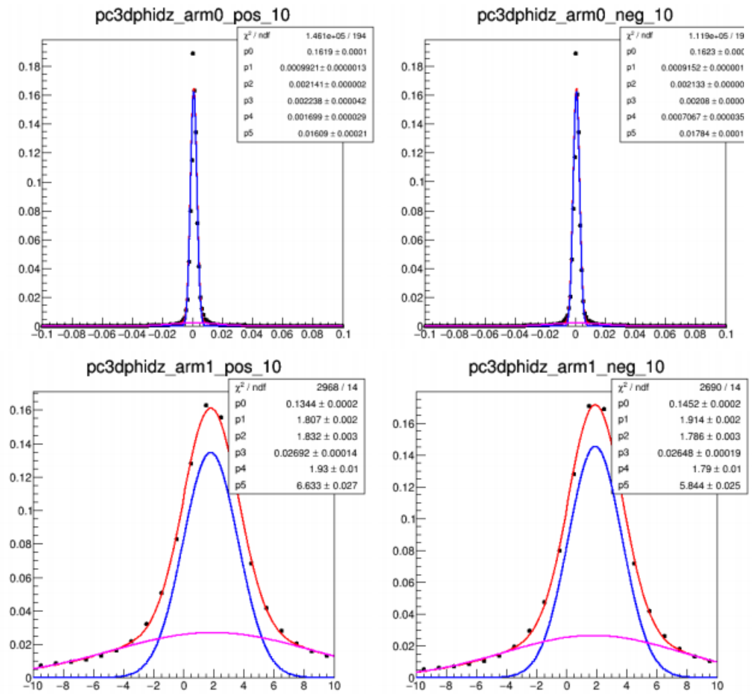

Figure 1.5: The top plots show the PC3 matching dϕ fit in range $1.0 < pT < 1.1$ (GeV/c). The blue and pink lines are single Gaussian fits to the signal and background, respectively, which are combined in the red line. The bottom plots show the result of the dz sigmalization, done in the same way as for dϕ.

the p+Aucollision system's inherent asymmetry, the majority of particles are produced in Au-going (i.e., south) direction. Taking into account this asymmetry, only the clusters from the south arm are used for calculations in this analysis. In a typical 0-5% centrality event, there are on average 1500 FVTX clusters in the south arm alone.

1.1.3 BBC PMTs

The BBC provides information on the position, time of arrival, and number of charged particles that hit the BBC's quartz radiator material. The BBC acceptance is $3.1 < |\eta| < 3.9$ and spans the full azimuth. The resolution of the detector in x and y is 5 cm, corresponding to the diameter of a BBC PMT. As with the FVTX, the z resolution is simply the width of the active area of the BBC divided by $\sqrt{12}$. In addition to spatial information, the BBC provides charge

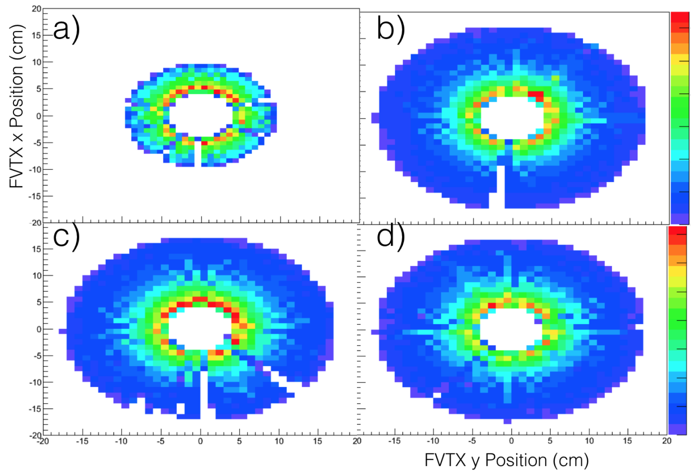

Figure 1.6: Distribution of FVTX clusters in x and y for layers 1, 2, 3, and 4 for panels a), b), c), and d), respectively. The color scale corresponds to the number of counts.

information, calibrated so that a value of 1.0 corresponds to a single charged particle hitting the detector. Fig 1.7 shows the layout of the PMTs for the BBC. As discussed in section **??**, the information regarding arrival time and particle charge can be used to calculate the z-vertex of the collision.

1.2 The Event Plane Method

Some details of the event plane were given in Chapter 2 Section **??**. The goal of this thesis is to measure v_2, which is related to collective behavior as evidenced by correlations among particles. These correlations exist relative to the orientation of the collision. The event plane method measures the azimuthal anisotropy in final state particles. The event plane method uses final state particles to calculate the event plane angle from the data. A different set of final state particles are used to define the event plane and measure the v_2.

An event plane angle is defined for each harmonic, and is denoted as Ψ_n where n is the harmonic number. The definition for Ψ_n is related to the calculation of the Q-vector. For an event with N particles, define the flow vector $\vec{Q}$ as follows:

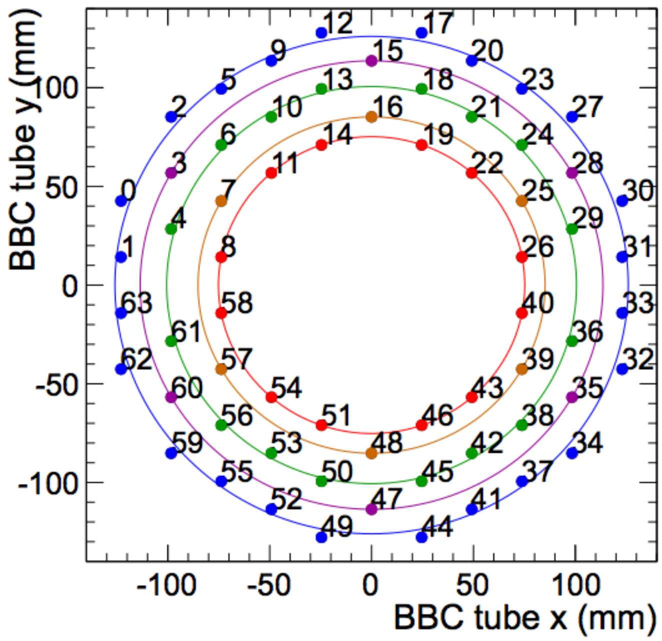

Figure 1.7: Diagram showing the positions of the PMTs for the BBC-south detector. Rings shown with the same color indicate PMTs at an approximate common radius.

$$Q_x = \sum_i^N (w_i * \cos(n * \phi_i)) \tag{1.3}$$

$$Q_y = \sum_i^N (w_i * \sin(n * \phi_i)) \tag{1.4}$$

$$Q_w = \sum_i^N (w_i) \tag{1.5}$$

where i is the ith particle in the event, ϕ_i is the azimuthal angle of the particle, w_i is the weight factor, and n is the harmonic number. We define the nth order event plane as $\Psi_n = \arctan\left(\frac{Q_y}{Q_x}\right)$.

Once the event plane has been calculated, the flow harmonics (v_n) are defined as

$$v_n = \frac{\langle\langle\cos(n(\phi - \Psi_n))\rangle\rangle}{Resolution(\Psi_n)}, \tag{1.6}$$

where $\langle\langle\rangle\rangle$ indicates that $\cos(2\phi - \psi)$ is averaged over all particles in the same event, and the resulting v_2 must be averaged over many events [25]. Note, the event plane angle and the q-vector are defined at the event level, v_2.

As discussed in Chapter 2, Section **??**, the event plane angle is a measurement which attempts to correspond to the physical reaction plane angle. Thus, the event plane is an imperfect representation of the reaction plane which needs to be corrected. This correction is known as the event plane resolution $Res(\Psi_n)$, and is calculated using the 3-subevent method. It is important to note the the set of particles used to calculate Ψ_n and ϕ must be different in order to avoid autocorrelations. This is usually done by imposing a large η gap (usually at least a half of a unit of pseudorapidity)between the two particle sets.

For this analysis, the event plane is calculated separately for each of the forward detectors mentioned above, i.e., the BBC and the FVTX. For the FVTX, the Q-vector is calculated in each event as

$$Q_x = \sum_{i}^{NClus} (\cos(n * \phi_i)) \tag{1.7}$$

$$Q_y = \sum_{i}^{NClus} (\sin(n * \phi_i)) \tag{1.8}$$

$$\phi_i = \arctan(\frac{Clus_y^i}{Clus_x^i}) \tag{1.9}$$

where NClus is the number FVTX clusters in that event and $Clus^i_{y,x}$ are the x and y components of the ith FVTX Cluster in that event. At this point, this Q-vector is calculated with no cluster dependent weight factor because each cluster is taken to be equal weight.

For the BBC, the Q-vector is calculated in each event as

$$Q_x = \sum_{i}^{N_{PMT}} (w_i \cos(n * \phi_i)) \tag{1.10}$$

$$Q_y = \sum_{i}^{N_{PMT}} (w_i \sin(n * \phi_i)) \tag{1.11}$$

$$Q_w = \sum_{i}^{N_{PMT}} (w_i) \tag{1.12}$$

$$\phi_i = \arctan(\frac{PMT_y^i}{PMT_x^i}) \tag{1.13}$$

where w_i is the charge collected on the PMT and N_{PMT} is the number of PMTs that fired (above threshold) in each event.

Finally, the v_n are calculated using a combination of the BBC or FVTX Q-vectors and the CA tracks as

$$v_n = \frac{\left\langle\left\langle \cos(n(\phi^{CA} - \Psi_n^{BBC,FVTX})) \right\rangle\right\rangle}{Resolution(\Psi_n^{BBC,FVTX})}. \tag{1.14}$$

In this analysis, we are concerned only with measuring the second-order harmonic v_2.

1.2.1 Event Plane Resolution Calculation

As mentioned above, the event plane resolution is calculated using the standard 3-subevent method[25]. The strategy of this method is to measure Ψ_2 with three different detectors in the same event, in order to better constrain the overall measurement of Ψ_2. The event plane resolution is defined as

$$Res(\Psi_2^A) = \sqrt{\frac{\left\langle \cos(2(\Psi_2^A - \Psi_2^B)) \right\rangle \left\langle \cos(2(\Psi_2^A - \Psi_2^C)) \right\rangle}{\left\langle \cos(2(\Psi_2^B - \Psi_2^C)) \right\rangle}}, \tag{1.15}$$

where A,B, and C are three detectors measuring the same event. Here, the term "subevent" refers to the specific subset of particles measured by a given detector, assuming no decorrelation [25].

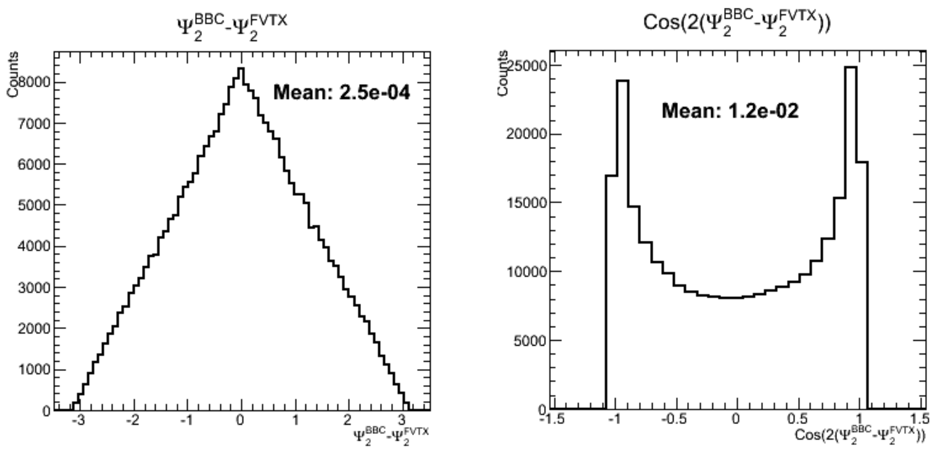

Figure 1.8: Intermediate steps involved in calculating the event resolution. (left) Raw difference between the event plane angles for two different detectors. This distribution is triangular because it is the result the cross-correlation of two uniform distributions, Ψ_2^{FVTX} and Ψ_2^{BBC}. (right) The cosine of two times the difference between the two event plane angles. The average of this distribution is used in equation 1.15.

In this analysis, the three detectors used to provide the required three subevents are the

FVTX-south, the BBC-south, and the CA, which span pseudorapidity acceptances of $-3 < \eta < -1$, $-3.9 < \eta < 3.1$, and $|\eta| < 0.35$, respectively. Unlike the BBCS and the FVTXS, the CNT detector does not have full azimuthal acceptance coverage. Therefore, the event plane angle cannot be reliably calculated with this detector for events whose event plane points outside of the acceptance. In order to solve this problem, we calculate the event plane resolution using a different, yet mathematically equivalent formulation that does not make use of $\psi_C NT$, as given below:

$$Res(\Psi_n^A) = \sqrt{\frac{\langle\langle \cos(n(\Psi_n^A - \phi^{CNT}))\rangle\rangle \, \langle \cos(n(\Psi_n^A - \Psi_n^C))\rangle}{\langle\langle \cos(n(\phi^{CNT} - \Psi_n^C))\rangle\rangle}}, \tag{1.16}$$

where there is a double average over each CNT track and each event.

Table 1.4:

Detector	$n = 2$	$n = 3$
FVTXs	0.216	0.010
BBCs	0.052	0.010

1.2.2 Event Plane Flattening Calibration

In order for the event plane to be useful in making a v_n measurement, the event plane angle must be calibrated such that its distribution is uniform. For the event plane method, a physical assumption is made that the true distribution of Ψ_n angles will be uniform. In other words, there is no preferred event plane angle in heavy ion collision. If the measured Ψ_n distribution is not flat, we attribute that behavior to variations in the efficiency of detecting charged particles as a function of ϕ. Thus, the event plane calibration procedure seeks to correct for these non-uniformities in acceptance, and restore the Ψ_n distribution to the physical expectation of uniformity. We employ a procedure to re-center and flatten the measured non-uniform Ψ_n distribution, such as the one shown in Figure 1.2.2.

The red curve in Fig. 1.2.2 depicts a significant deviation from uniformity in the Ψ_2 distribution. The flattening calibration attempts to correct for this lack of uniformity by shifting the Ψ_2 value of each individual event by an amount corresponding to the deviation of the overall distribution for all events. Although this procedure results in a uniform Ψ_2 distribution, applying too large of a correction arising from an exceedingly distorted initial distribution can lead to systematic effects on the v_2 measurement, which will be discussed in the next section. Therefore, it is important to address any systematic effects that would affect the uniformity of the Ψ_2 distribution.

The flattening calibration requires two steps to completely flatten the Ψ_n distribution. The first step of the calibration is to re-center the mean of the raw Ψ_n distribution to be at 0.0 radians and to resize the RMS. The second step is to Fourier transform the re-centered distribution and use the transformation to shift the Ψ_n values to a uniform distribution. With flattening, each Ψ_n is transformed to $\Psi_n + \Delta\Psi_n$. $\Delta\Psi_n$ is defined as

$$\Delta\Psi_n = \sum_{i=1}^{N} \left(\frac{2}{i} \left(\sin(i\Psi) F_i^{\cos}(f(\Psi_n)) - \cos(i\Psi) F_i^{\sin}(f(\Psi_n)) \right) \right), \tag{1.17}$$

where N is the number of components, $F_i^{\cos}(f(x))$ is the ith component of the cosine Fourier transform of $f(x)$, and $f(\Psi_n)$ is the Ψ_n distribution. For this analysis, N =12 is a sufficient number of components to flatten the Ψ_n distribution. The re-centering and flattening calibration is done in separate 30 z-vertex bins.

1.3 East West v_2 Discrepancy

As discussed in the previous section, distortions in the raw Ψ_2 distribution can cause distortions in the measurement of v_2. In this section, we discuss how the beam alignment effects the raw Ψ2 distribution and how it can be corrected for.

As shown in Fig 1.10, v_2 is different when measured using tracks in the west (-1 $< \phi <$ 1) and east arm (2 $< \phi <$ 4) of the CA. This is a systematic effect explained by the colliding beams not being parallel to the longitudinal axis of PHENIX. When examining beam alignment effects on the v_2 measurement, we can quantify the east west v_2 asymmetry by calculating R_{v_2} which is

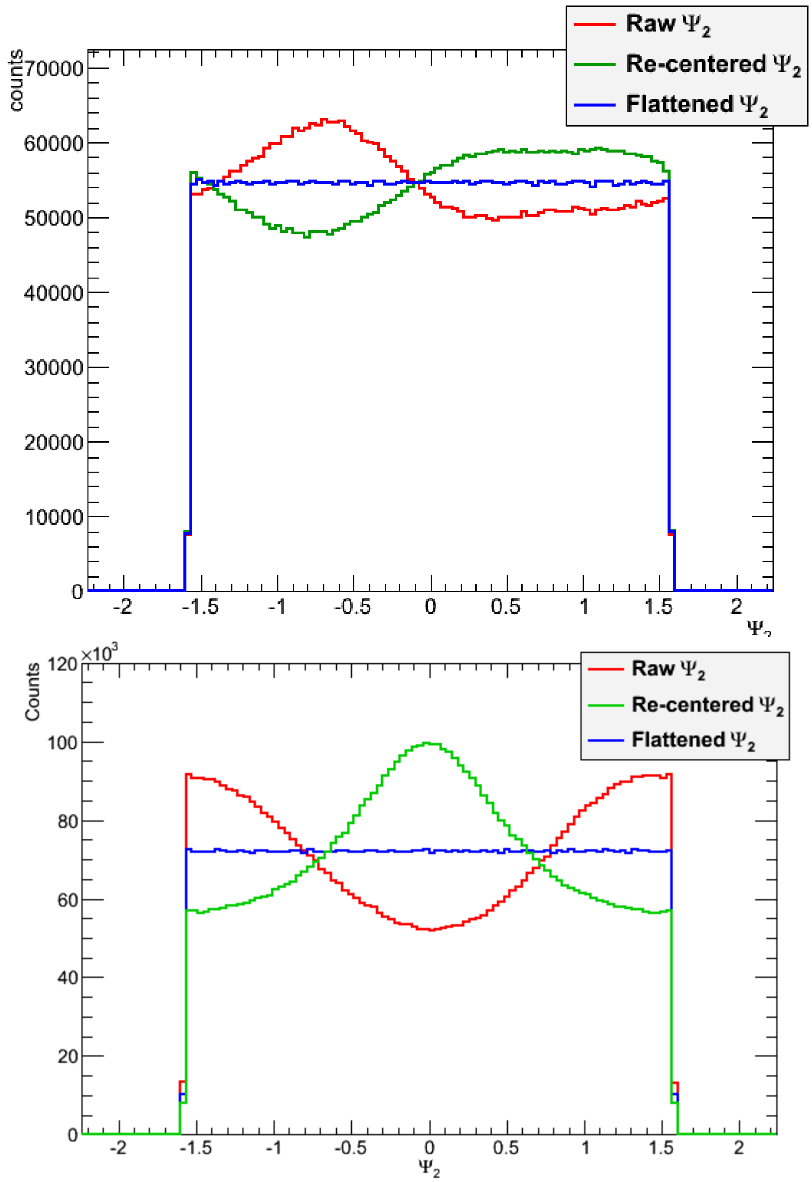

Figure 1.9: This is the Ψ_2 distribution projected over all z-vertex bins at different steps during the calibration. The top is from the FVTX south and the bottom is from the BBC south. The range of the Ψ_2 resolution is from -$\frac{\pi}{2}$ to $\frac{\pi}{2}$ because of the periodicity. The raw (in red) Ψ_2 distribution has a sinusoidal shape. The re-centered (in green) Ψ_2 distribution moves the mean. The flattened (in blue) Ψ_2 distribution spreads out the counts so that there is uniformity. Each calibration step preserves the integral.

calculated by:

$$R_{v_2} = \frac{\sum_{p_T} v_2^{east}(p_T)}{\sum_{p_T} v_2^{west}(p_T)}. \tag{1.18}$$

In Figure 1.12, $R_{v_2^{FVTXs}}$ can be extracted by taking the ratio of the numbers in the legend of the

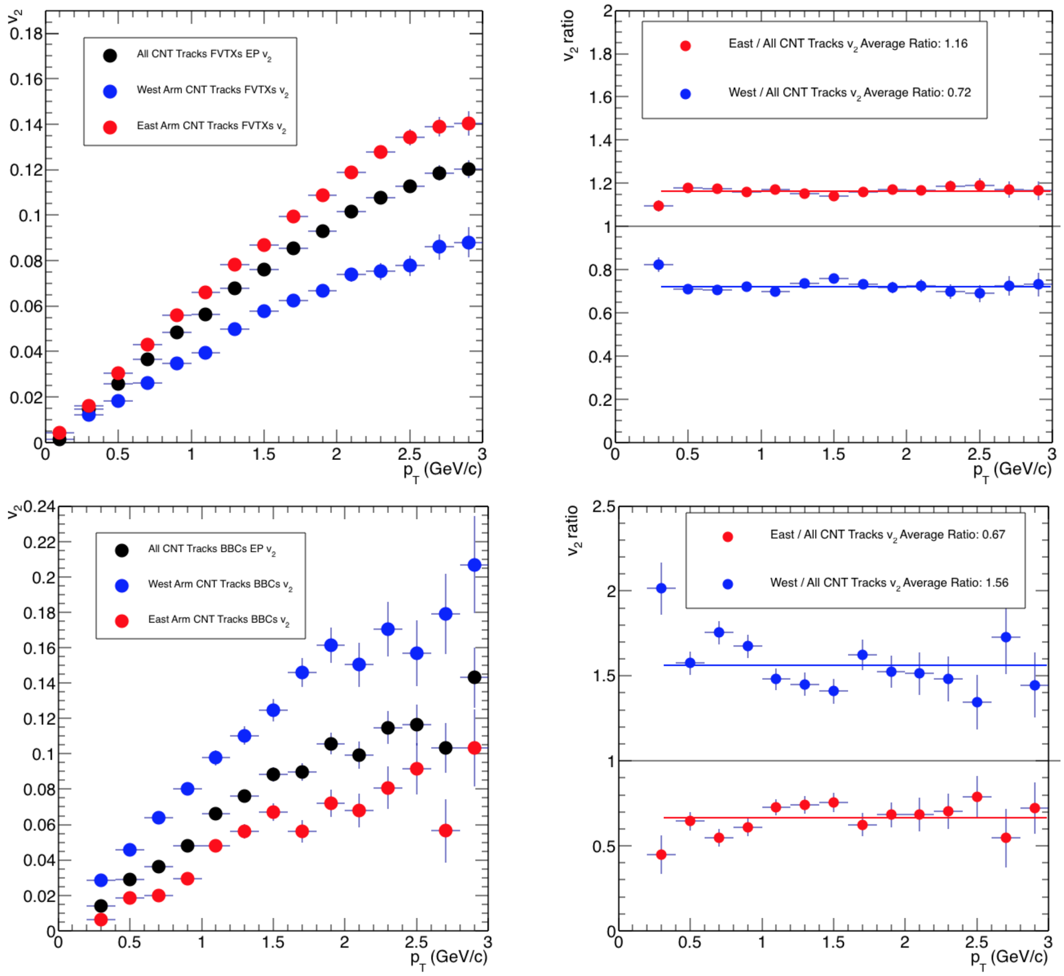

Figure 1.10: First attempt at measuring $v_2(p_T)$ with the event plane as calculated with the FVTXs (top left) and the BBCs (bottom left) in the p+Au at $\sqrt{s_{NN}}$= 200 GeV dataset, using the default resolution as shown in Table 1.4. The black points show v_2 measured using all CNT tracks. The blue and red points show v_2 measured using only tracks in the west and east arms, respectively. The ratios are fit with a constant, whose value is shown in the legend.

upper right plot and $R_{v_2^{BBCs}}$ can be extracted the same way for the numbers in the bottom left plot's legend. The $R_{v_2^{FVTXs}} = 1.61$ while the $R_{v_2^{BBCs}} = 0.43$, indicating large east west asymmetry in both measurements, although the $R_{v_2^{BBCs}}$ is bigger. It is interesting to note that the splitting of the east and west v_2 measurements goes in opposite directions for the BBCs as opposed to the FVTXs. To understand where the discrepancy in these v_2 measurements comes from, we examine the effects of the beam alignment on the v_2 measurement.

1.4 Correcting for the Effects of Beam Alignment

First of all, the collision vertex is significantly offset from the z-axis to which all of the PHENIX detectors are aligned. The other beam geometry effect, and the more significant of the two effects, comes from the fact that the beams are colliding at an angle of 3.6 milli-Radians in the x-z plane as show in Fig 1.11 [3]. The reason a non-ideal beam geometry creates an east west v2 measurement difference is because of the assumption that the ideal event plane angle is azimuthally isotropic during the event plane flattening calibration. In the translated and rotated frame where the beams are aligned with the z-axis the event plane distribution would be uniform, but in the lab frame the event plane distribution in ϕ would have regions of enhancement and reduction. The event plane flattening calibration algorithm restores a non-uniform distribution to a uniform one; however, if the true event plane distribution is non-uniform then forcing the measured distribution to be uniform would produce systematic errors.

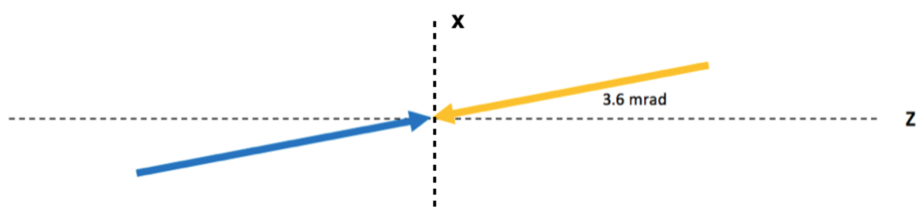

Figure 1.11: Diagram illustrating the angle at which the yellow and blue beams collide relative to the longitudinal $z-$axis of the detector. The yellow beam corresponds to the Au (south-going) beam, and blue corresponds to the proton (north-going) beam. Due to a necessity of running p+Au collisions at $\sqrt{s_{NN}}$= 200 GeV at RHIC, the beams collide at an angle of 3.6 mrad.

We correct for the offset of the collision vertex by shifting the origin of the PHENIX global coordinate system to the true collision vertex. To correct for the effect of the beam angle, we apply a global rotation of the PHENIX coordinate to align its longitudinal axis with that of the beams. In practice, these transformations are accomplished by individually applying a global rotation and translation to every CA track, FVTX cluster, and BBCs PMT.

As shown in Fig 1.12, applying these corrections prior to calculating v_2 reduces the magnitude of the east-west discrepancy. The new $R_{v_2^{FVTXs}} = 1.43$, while the $R_{v_2^{BBCs}} = 0.66$, which is a reduction from east-west difference measured without any corrections. However, even after rotating the PHENIX global coordinate system to be in alignment with the beam axis, due to the fact Ψ_2 is a derived quantity, there is a residual effect from the beam rotation which still effects the v_2 measurement.

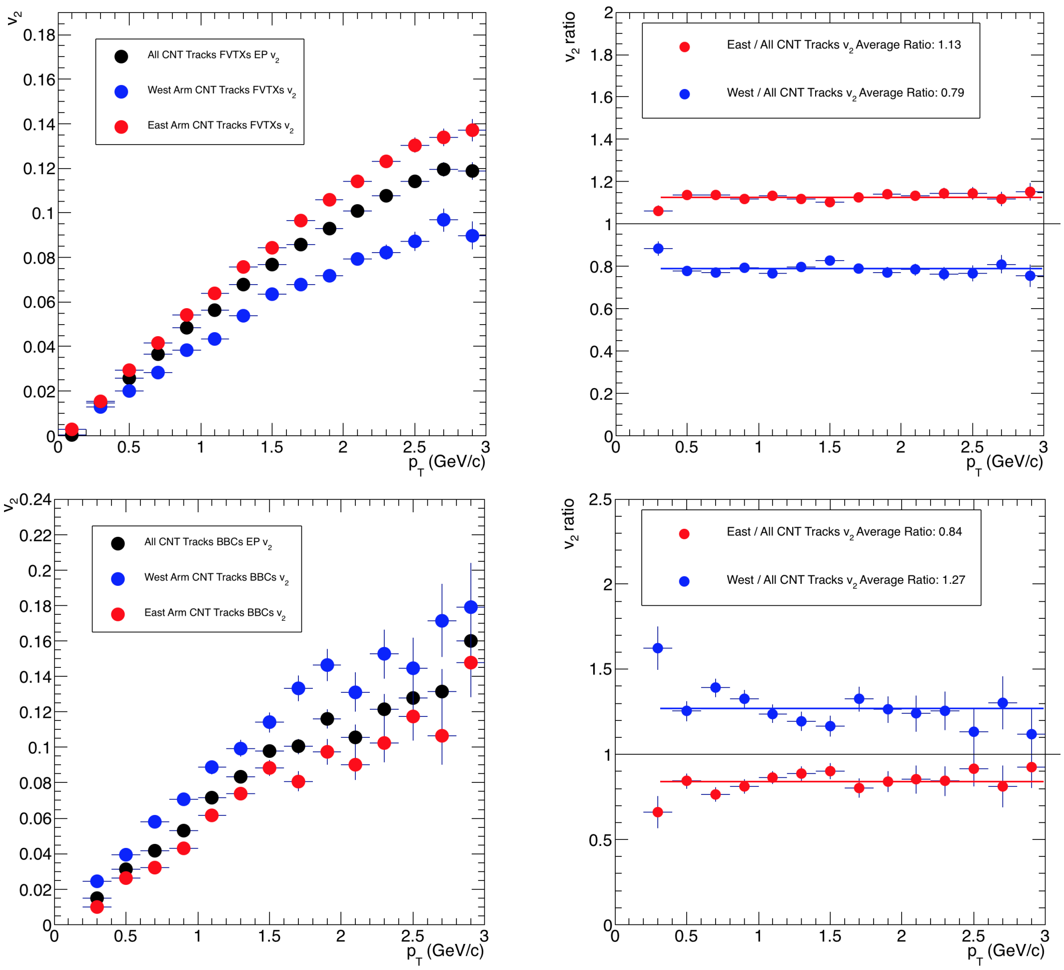

Figure 1.12: A corrected measurement of v_2 as a function of p_T with the FVTXs (top two panels) and the BBCs (bottom two panels) event plane for the p+Au $\sqrt{s_{NN}}$= 200 GeV dataset. The default resolution as shown in table 1.4 is used. The plotting conventions are the same as described in the caption of Fig 1.10.

To explain this effect, consider a cylindrical disk with a hole in the middle, centered about the z-axis (in analogy to the shape of the FVTX and the BBC), as shown in the left plot of Fig 1.13. In this geometry, all points along a ring of constant radius are at the same pseudorapidity. However, if one were to tilt that disk, the pseudorapidity of points along that ring would be ϕ dependent. The tilt of the disk changes its pseudorapidity acceptance and its extent. Now consider that it is not the disk that is tilted but rather the beam orientation that is tilted. The previous statements about the effect on the η range being ϕ dependent still apply.

The combination of the η acceptance changing, and the η distribution of charged particles not being flat means that the average amount of charged particles going through the disk would be systematically ϕ dependent, as illustrated in Fig 1.13. If the average charged particle distribution is not uniform in ϕ, the event plane distribution will not be either. This results in the flattening procedure creating systematic effects such as the east-west v_2 asymmetry.

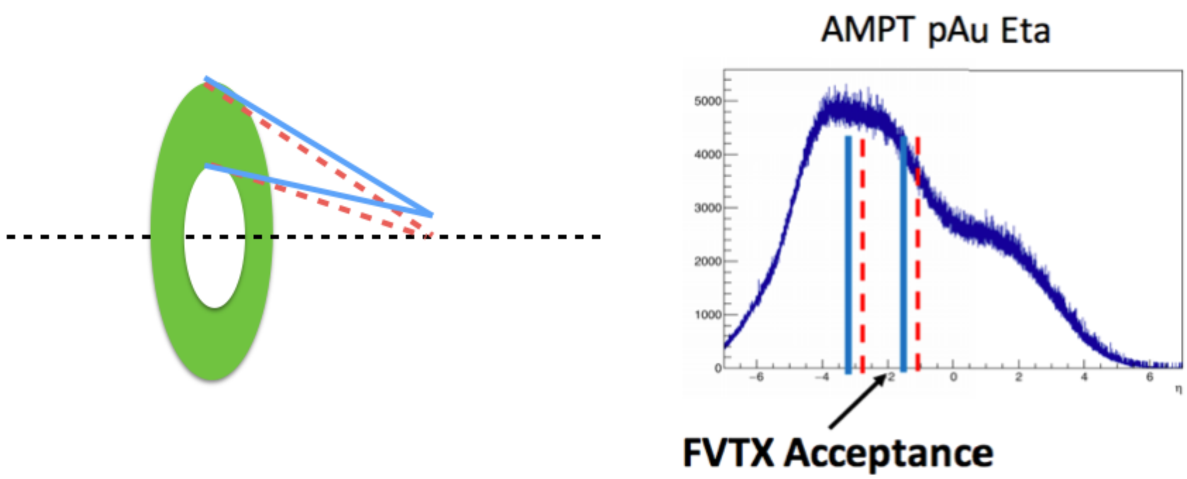

Figure 1.13: (left) Cartoon diagram illustrating η acceptance shift due to a beam offset in one of the FVTXs layers. (right) Pseudorapidity distribution of charged particles from the AMPT Monte Carlo generator for p+Au $\sqrt{s_{NN}}$= 200 GeV, showing the shift in η acceptance.

In order to correct for this effect, an additional weight factor is introduced for FVTX clusters and BBC PMTs during the event plane calculation. This factor is such that hits in ϕ regions with systematically less particles are given a larger weight, and correspondingly, hits in ϕ regions with systematically more particles are weighted less. The introduction of this weighting as defined below does not formally change the event plane calculation, as a weight factor is already implemented in its construction. The modified weight factor is:

$$w_i = w_i^D * F(\phi, Vertex_Z) \tag{1.19}$$

where w_i^D is the default weighting associated with the detector element, and $F(\phi, Vertex_Z)$ is the multiplicative weighting to correct for the beam geometry. $F(\phi, Vertex_Z)$ is dependent on $Vertex_Z$, in addition to ϕ, because η is dependent on the collision vertex. One can analytically calculate this ϕ dependent weight factor using the geometry of the FVTXs and BBCs as well as using the η distribution of charged particles. Unfortunately, the η distribution of charged particles in p+Au $\sqrt{s_{NN}}$= 200 GeV has not been measured by an experiment, so we must rely on models that may be inaccurate.

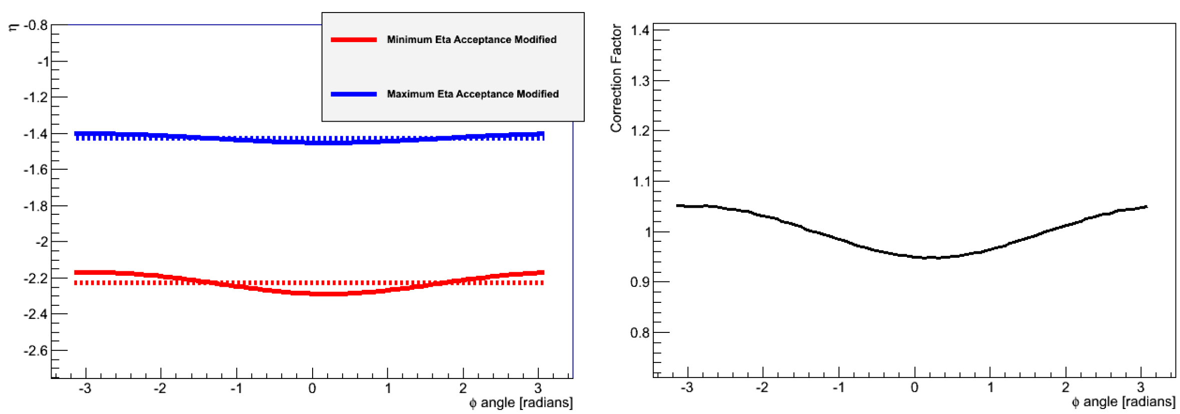

Figure 1.14: The left is the modification of the η acceptance as a function of ϕ for the FVTX first layer. The right is the calculated correction factor from this modification.

Another way to determine the weight factor is to use a data driven method of measuring to what extent each ϕ region in a detector has systematically more or less particles. Then an inverse weighting based on this measurement is applied to the ϕ regions to correct the detector's ϕ distribution to uniformity. The precise implementation of measuring and applying the uniformity of the ϕ regions in a detector will be examined further in the following sections.

1.4.1 FVTX Inverse Phi Weighting

For this method, the weight factor is determined by plotting all hits in a cylindrical disk detector vs ϕ, normalizing this distribution to one, and then inverting it. Applying this weight factor to the data will produce uniform hit distributions in ϕ in the detectors in which it is applied. This will, in turn, make the event plane distribution more uniform when measured in those detectors, thus correcting for the effect. The added benefit of using this method is also correcting for hot and cold ϕ regions in the detector. In order to get rid of significant hot or cold ϕ regions, ϕ regions with weight factors greater than 1.5 or less than 0.5 are set to 0.0. This correction is done for each FVTX layer, in z-vertex bins, and per run. The multiplicative weight function $F(\phi, Vertex_Z)$ for the FVTX disks is defined as

$$F(\phi, Vertex_Z, layer) = \frac{\langle N_{CLUS}(Vertex_Z, layer)\rangle}{N_{CLUS}(\phi, Vertex_Z, layer)}, \tag{1.20}$$

where $N_{CLUS}(\phi, Vertex_Z, layer)$ is the number of FVTX clusters as a function of ϕ, $Vertex_Z$, and FVTX layer and $\langle N_{CLUS}(Vertex_Z, layer)\rangle$ is the ϕ average of the number of clusters. The weighting can be seen in Fig 1.15. A comparison between the FVTX weighting and the analytic correction is shown. The good agreement indicates the validity of the weighting.

1.4.2 BBC Charge Weighting

For the BBC, we used another data driven method to correct for the non-uniform particle distribution. Using the distribution of particles in the BBC from the 2015 p+p $\sqrt{s} = 200$ dataset as a baseline, we applied an inverse weighting much like the method described in the previous paragraph. In the p+p dataset, there was no issue with beam colliding at an angle and the average charge across all 64 PMTs in the BBCs is uniform. In this method, the multiplicative weight function $F(PMT, Vertex_Z)$ for the BBCs is defined as:

$$F(PMT, Vertex_Z) = \frac{\left\langle N^{p+p}_{Charge}(Vertex_Z)\right\rangle}{\left\langle N^{p+Au}_{Charge}(PMT, Vertex_Z)\right\rangle}, \tag{1.21}$$

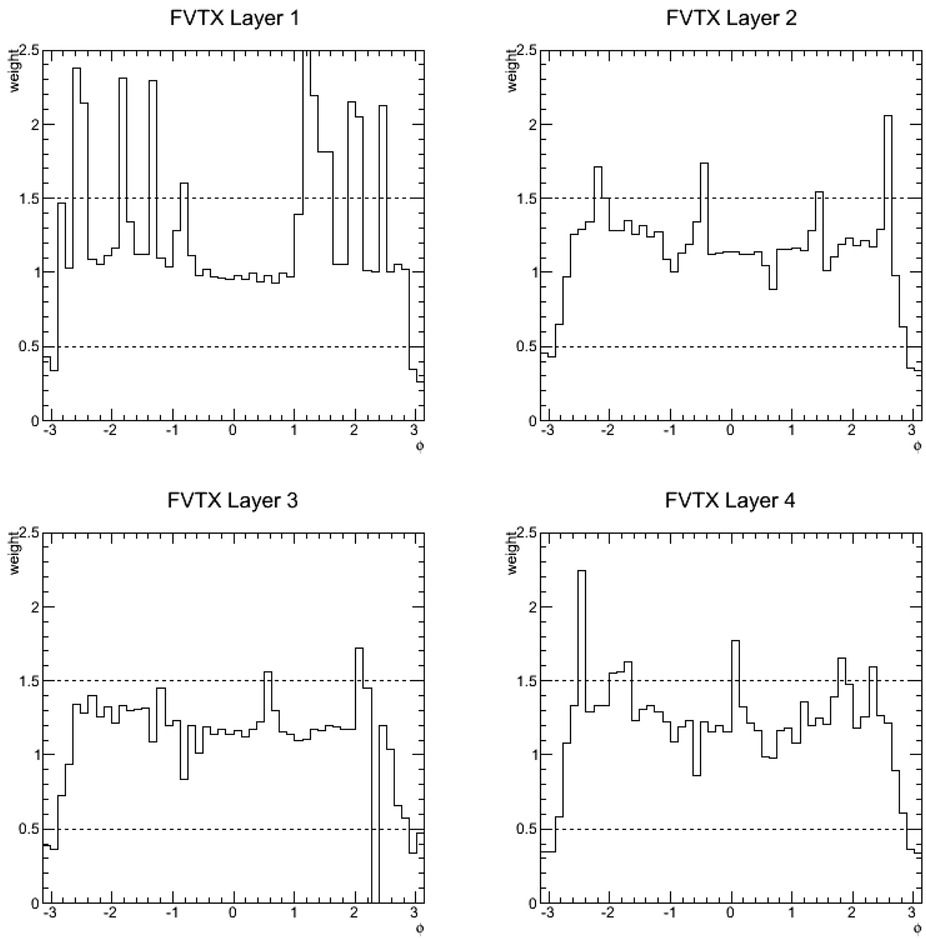

Figure 1.15: These four panels show the FVTX ϕ dependent cluster weighting when calculating the FVTX event plane for each layer separately for events with a collision vertex in z is around 0. There are some ϕ regions where weight factor is outside of the dotted line bounds. This indicates that either there was a severe deficit or excess of clusters measured in the region. Later, we will examine the effect of keeping these regions or cutting them out on the v_2 measurement.

where $< N_{Charge}^{p+p,p+Au}(PMT, Vertex_Z) >$ is the event averaged charge as a function of PMT and $Vertex_z$ for the p+p and p+Au datasets respectively. This weight function is shown in Fig 1.17 and is applied directly to the event plane calculation using Eqns 1.19 and 1.13. Although the weight function could be defined as a function of ϕ like in the FVTX case, the positions of the PMTs in the BBC are fixed and it is more direct to take the ratio between PMTs.

One effect of using this weighting method is that it will make the distribution of particles in the BBC in ϕ and η uniform. This can be illustrated by looking at Fig 1.18. It is apparent that the

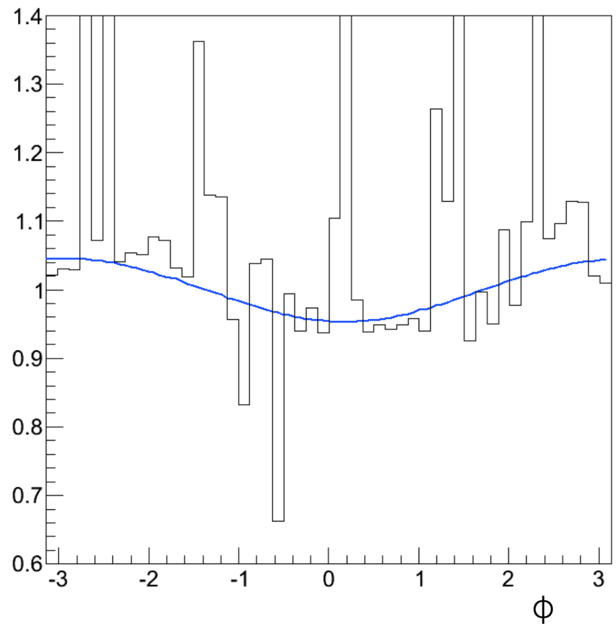

Figure 1.16: The black is the FVTX weighting and the blue is the analytic weighting. They have good agreement.

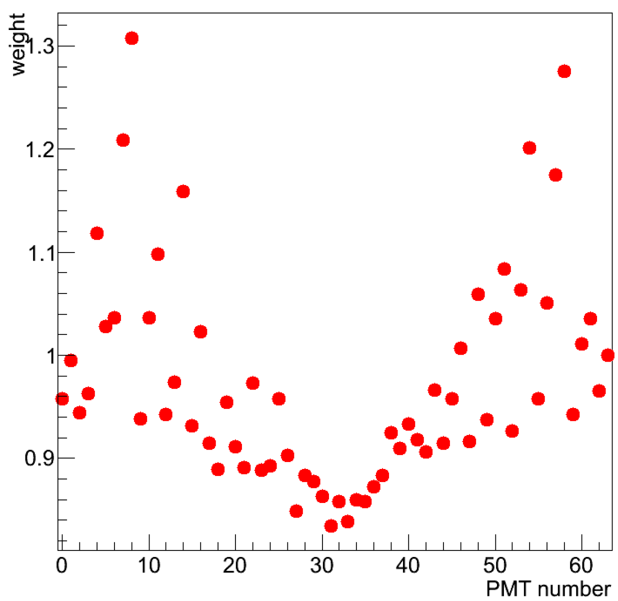

Figure 1.17: Shown here is BBC the multiplicative weight factor F used when calculating the modified event plane for events where the collision vertex in z is around 0. The y-axis is the weight factor and the x-axis is the PMT number for the BBCs (there are 64 total in the BBCs).

p+p average charge is much more uniform than the p+Au average charge as a function of ϕ and ring. After applying the p+p/p+Au ratio weighting, which is essentially dividing the left plot by the right plot in Fig 1.18, the PMT charges in ring 1 for the p+Au dataset will be deweighted so that their corrected average charge will be uniform in ϕ, and in agreement with the average charge for the other rings. If all the BBC rings have the same average charge, this means that the average charge as a function of η for the BBC will be approximately uniform. This is one reason why this method (p+p/p+Au ratio weighting) is preferred for the BBC, because the variations in the average charge between the rings are normalized. One could apply the FVTX method of inverse ϕ weighting by inverting the right plot of Fig 1.18 to find the weight function. However, although using only the p+Au dataset would normalize the average charge as a function of ϕ, it would not normalize the charge as a function of η. Both methods applied to the data are shown in the next section but the p+p/p+Au ratio method does better.

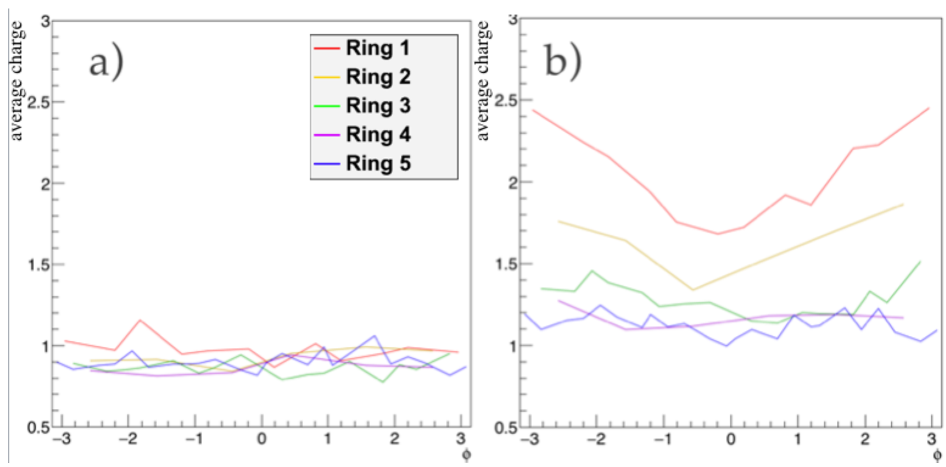

Figure 1.18: These plots depict the average PMT charge per event versus ϕ in the a) the p+p $\sqrt{s}=$ 200 GeV and b) p+Au $\sqrt{s_{NN}}=$ 200 GeV. The PMTs are separated by color, which corresponds to the rings of approximate common radius as shown in Fig 1.7. The left plot shows near uniformity as a function of ϕ and ring. However, the right plot shows a significant deviation from uniformity especially for the innermost rings (rings 1 and 2). In addition to the ϕ variation for the right plot, the innermost rings have the largest average charge when compared to the other rings. This is in part due to the fact the innermost rings cover the a slightly larger η range. However, the innermost rings in the left plot also cover the largest η range and do not exhibit this separation in rings.

1.4.3 Applying Weighting to v2

The previously discussed corrections are applied when calculating the raw Ψ_2^{FVTXs} used in the v_2 measurement. Shown in Figure 1.19 is the correction summary for the FVTXs v_2 measurement where $R_{v_2^{FVTXs}}$ is the y-axis. The first column, which corresponds to $R_{v_2^{FVTXs}}$ calculated using FVTXs layers 1, 2, and 4, with layer 3 being excluded, is explained shortly. The black, red, blue, and green points correspond to no weighting, analytic weighting, inverse ϕ weighting, and inverse ϕ weighting with cuts, respectively. Compared to the $R_{v_2^{FVTXs}}$ calculated with no weighting, $R_{v_2^{FVTXs}}$ calculated with each of the corrections brings the ratio quantity much closer to 1.0, indicating the weighting techniques are working. In order to better understand the effect of the corrections, $R_{v_2^{FVTXs}}$ is measured separately with each FVTXs layer. The rationale for this exclusion is due to FVTXs layer 3's unusual behavior in relation to the other FVTXs layers. As we go from layer 1 to layer 4, the $R_{v_2^{FVTXs}}$ generally is trending downward except for layer 3. Although the reason for this was never definitively determined, it is likely there is something wrong with the layer data due to electronic or detector problems. Thus, the measurement of v_2^{FVTXs} is calculated without any clusters in the third layer.

Similarly, Figure 1.20 is the correction summary for the BBCs v_2 measurement where $R_{v_2^{BBCs}}$ is the y-axis. The first column corresponds to $R_{v_2^{BBCs}}$ calculated using all five BBCs rings. Compared to the $R_{v_2^{BBCs}}$ when calculated with no weighting, $R_{v_2^{BBCs}}$ when calculated with the data driven and p+p/p+Au ratio weighting is modestly closer to 1.0. By looking at $R_{v_2^{BBCs}}$ calculated with PMTs in individual BBCs rings for the weighted points, $R_{v_2^{BBCs}}$ is generally trending downward as a function of ring number. Applying the weighting corrections to $R_{v_2^{BBCs}}$ calculated by ring 1, the innermost ring, over-corrects $R_{v_2^{BBCs}}$. This may be explained by the fact that ring 1 covers the largest η acceptance range, causing the correction to be inconsistent. The reason why ring 1 is not excluded from the inclusive v_2 calculation, like FVTXs layer 3 excluded, is because there is no reasonable justification to exclude it other than its over-corrected $R_{v_2^{BBCs}}$ values. While FVTXs layer 3 breaks the trend of $R_{v_2^{FVTXs}}$ decreasing, BBCs ring 1 follows the $R_{v_2^{BBCs}}$ ring trend.

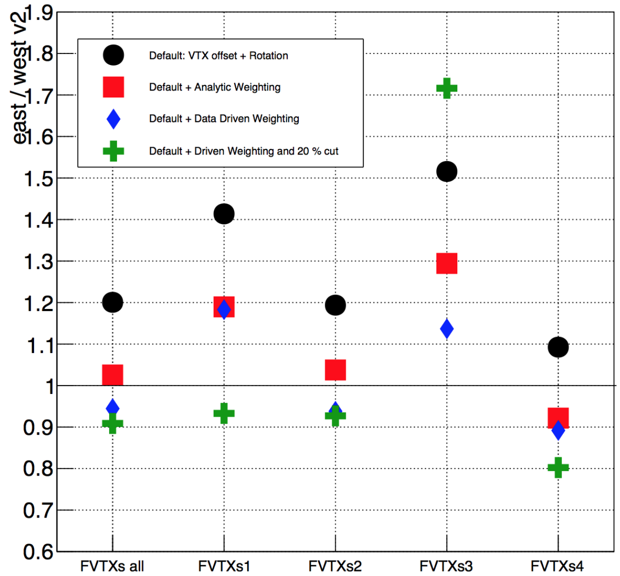

FVTXs All using layers 1, 2, and 4

Figure 1.19: Plotted is the FVTXs correction summary where the y-axis is the east/west v_2 ratio and the x-axis is the different subset of clusters used to calculate the v_2. The black markers correspond to the default corrections. The red boxes correspond to the corrections with the analytic weighting shown in Fig 1.14. The blue diamonds are the FVTX inverse ϕ weighting as shown is section 1.4.1. Finally, the green crosses correspond to the same as the blue diamonds except an additional hot-cold filter of 20% was applied. The first column is using all the FVTXs layers except for the 3rd layer (explained in the text). So the first columns should be approximately the average of columns 2, 3, and 5. Columns 2 through 5 show the ratio calculated from clusters only in that layer.

Fig 1.21 shows the $v_2(p_T)$ with the inverse ϕ weighting and 20 % cut from Figure 1.19. This figure also shows $v_2(p_T)$ with the pp/pAu ratio weighting from Fig 1.20. Although the east and west v_2^{BBCs} measurements do not collapse together like the east and west v_2^{FVTXs} measurements, the result is good enough to reduce our systematics uncertainty. Due to the fact that $R_{v_2^{FVTXs}}$ is corrected to within $\pm 10\%$ and the fact that $v_2^{FVTXs}(p_T)$ has smaller a statistical uncertainty, the primary $v_2(p_T)$ measurement is done using the FVTXs.

1.5 Systematic Uncertainties

The dominant systematic uncertainties associated with the $v_2(p_T)$ measurement are as follows: (1) track background from photonic conversions and weak decays, which we estimate at 2%

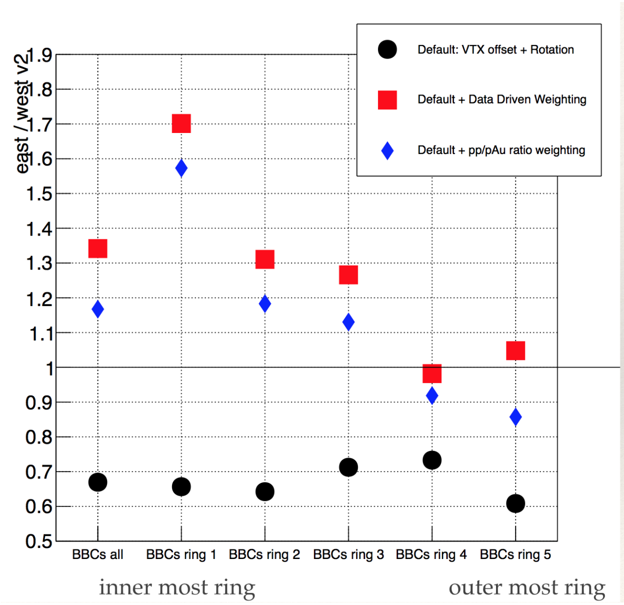

Figure 1.20: Plotted is the BBC correction summary where the y-axis is the east/west v_2 ratio and the x-axis is the different subset of PMTs used to calculate the v_2. The black markers correspond to the default corrections. The red boxes correspond to the corrections with the analytic weighting shown in Fig 1.14. Finally, the blue diamonds correspond to the BBC inverse ϕ charge weighting as shown is section 1.4.2. The first column is the quantity calculated from all PMTs. Columns 2 through 6 are using PMTs from certain rings as defined in Fig 1.7. Ring 1 is the hardest to correct. The first column should approximately be the average of all the other columns.

relative to v_2 by varying the windows in the PC3 matching variables from 3σ to 2σ; (2) many collisions occurring in the same bunch crossing, that occur at a rate of 8% in 0-5% central p+Au collisions. Low-luminosity and high-luminosity subsets of the data were analyzed, and the systematic uncertainty was determined to be $^{+4\%}_{-0\%}$, since the v_2 was found to decrease in the events that contain a pile-up; (3) non-flow correlations which enhance the v_2, whose contribution we estimate from Fig. 1.24, assigning a p_T-dependent asymmetric uncertainty with a maximum value of $^{+0}_{-23}\%$; (4) as discussed in the previous section, the beam alignment effects on the determination of Ψ_2. We assign a value of 5% for this systematic uncertainty by taking the difference of v_2 when measured independently in the east and the west arms after applying the necessary corrections; (5) the difference in the $v_2(p_T)$ values when measured independently using the BBCs and FVTXs event planes, which differ by $\pm 3\%$.

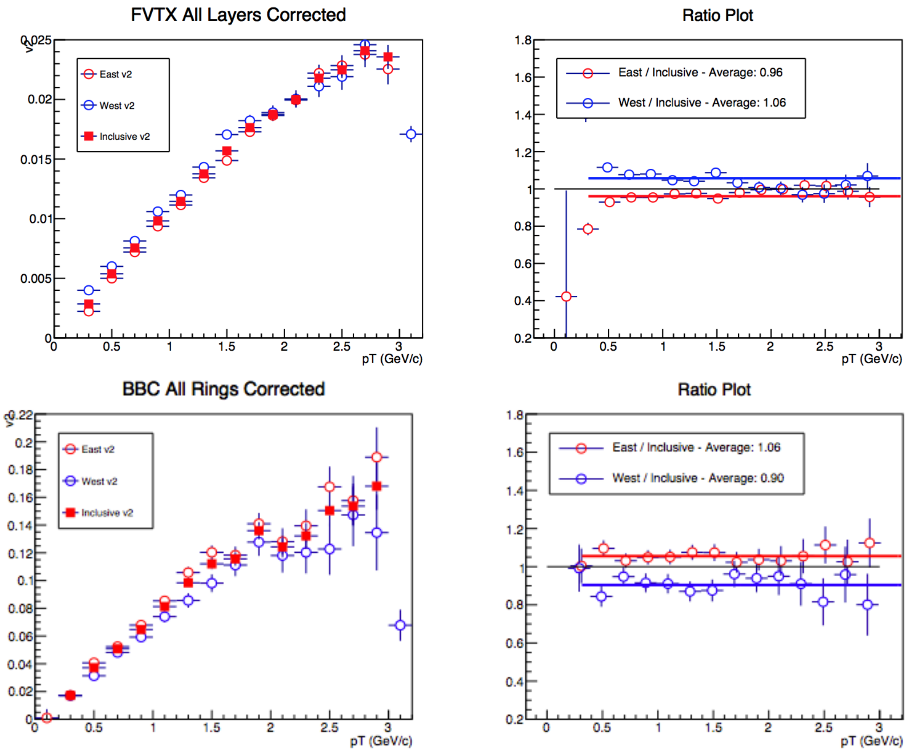

Figure 1.21: FVTXs v_2 event plane measurement corrected with inverse ϕ weighting and 20 % cut with FVTXs layer 3 is excluded (top) and BBCs v_2 event plane measurement corrected with p+p/p+Au ratio weighting (bottom).

Table 1.5 summarizes of all these systematic uncertainties, categorized by type:

(1) point-to-point uncorrelated between p_T bins,

(2) point-to-point correlated between p_T bins,

(3) overall normalization uncertainty in which all points are scaled by the same multiplicative factor.

1.5.1 Effect of Event Pile-Up

Pile-up events occur when there are two or more collisions within the same bunch crossing. Pile-up events are an issue for this analysis because they:

Table 1.5: Systematic uncertainties given as a percent of the v_2 measurement. Note that the non-flow contribution is p_T dependent and the value here quoted corresponds to the highest measured p_T.

Source	Systematic Uncertainty	Type
Track Background	2.0%	1
Event Pile-up	$^{+4}_{-0}\%$	2
Non-Flow	$^{+0}_{-23}\%$	2
Beam Angle	5.0%	3
Event Plane Detectors	3%	3

(1) are erroneously included into the 0-5% centrality selection due to two smaller collisions looking like a larger collision,

(2) and reduce the value of v_2 because the event plane angle from one collision will be different than the event plane angle in the other collision, such that correlations calculated by using particles produced from the two collisions are random and will dilute the real correlations, thereby reducing the flow signal.

In order to filter pile-up events we look at the distribution of BBC PMT timing values as seen in Fig 1.22. A normal event is strongly peaked at 0 while a pile-up event has a broad distribution and may not be centered at 0. We can come up with an algorithm to efficiently filter pile-up events by analyzing the BBC PMT timing value distribution event by event. When the v_2 values are compared with and without the filter, a difference of 4% is seen.

1.5.2 Effects of Non-Flow

Non-flow is a catch-all term used to categorize all types of long-range angular correlations which do not arise from hydrodynamic flow and are not related to the initial collision geometry. Non-flow constitutes a significant background to our measurement. There are several known sources of non-flow:

(1) hard scattering events producing dijets

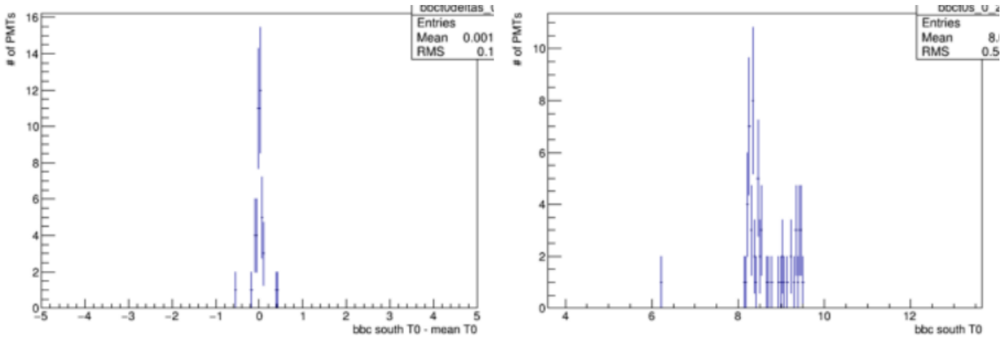

Figure 1.22: The distribution of BBC PMT timing values. The x-axis is the difference between the southern BBC PMT t_0 - the mean t_0 in the south. An example of a normal event (left) and an example pile-up event (right), are shown.

(2) initial state correlations between target and projectile

(3) decay chains of exotic particles

(4) momentum conservation.

Fig 1.23 shows the characteristic two-particle correlations arising from non-flow associated with dijets. The near-side peak at (0,0) is from the cone of particles in a single jet all at a similar location in η and ϕ. The away-side ridge around $\phi = \pi$ originates from particles pairs, where each particle belongs to a different jet. The two jets are completely back-to-back in $\Delta\phi$, but have a spread in $\Delta\eta$. This correlation function yields a substantial c_2 very similar to that from the hydrodynamic flow signal we are seeking. In order to minimize the contribution of dijet events, the standard flow analysis procedure is to select regions outside of the red dotted lines seen in Fig 1.23 ($|\Delta\eta| > \eta_{min}$, where η_{min} is usually of order 1.0 unit of pseudorapidity).

In order to estimate the degree of presence of non-flow, we can measure the c_2 from p+p events which should be devoid of any hydrodynamic flow but should have many of the sources of non-flow present. In order to compare p+p with p+Au, we must scale-up the p+p quantity by the dilution factor defined in eq 1.22. The scaled down reference c_2 is shown as blue squares in Fig. 1.24, panel (a). The ratio of c_2 in the scaled-down p+p reference to that in p+Au is shown in panel (b).

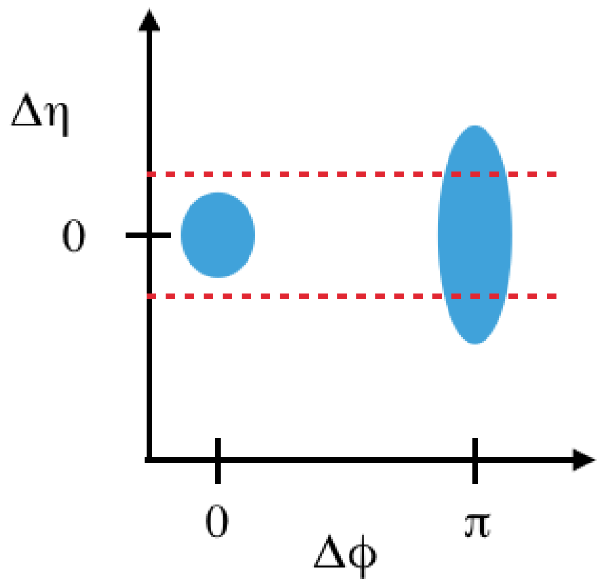

Figure 1.23: Plotted here is the 2D profile of a correlation function in $\Delta\eta\Delta\phi$ space of a dijet event. The area in red dotted lines represent the exclusion zone in $\Delta\eta$, such that the measurement is made only using data from outside of the exclusion zone to reduce non-flow contributions.

From this ratio, as calculated in 1.22, it can be seen that the relative correlation strength in p+Au from elementary processes is at most 23% at the highest p_T. Since this procedure constitutes an approximation to quantify the non-flow correlation strength, it is not subtracted from the total signal, instead it is treated as a source of systematic uncertainty. Even though the p+Au and the p+p baseline data were collected in different years, such that potential changes in detector performance could affect our results, it was verified that using p+p data from various run periods has an effect of at most 3% on the calculated non-flow contribution.

$$c_2^{\text{pAu elementary}}(p_T) \simeq c_2^{p+p}(p_T)\frac{\left(\sum Q^{\text{BBC-S}}\right)_{p+p}}{\left(\sum Q^{\text{BBC-S}}\right)_{\text{pAu}}}. \tag{1.22}$$

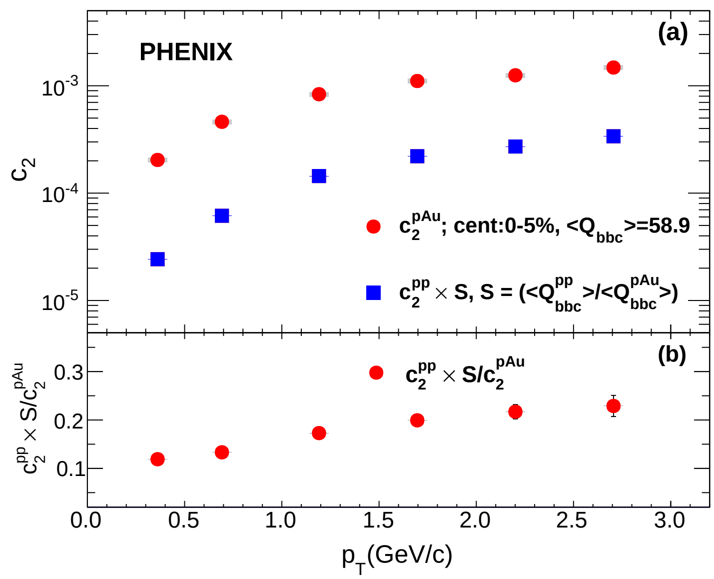

Figure 1.24: (a) The second order harmonic coefficients $c_2(p_T)$ for long range angular correlations in 0%–5% p+Au collisions, as well as for minimum bias p+p collisions. The latter are scaled down by the factor $\left(\sum Q^{\text{BBC-S}}\right)_{p+p} / \left(\sum Q^{\text{BBC-S}}\right)_{\text{pAu}}$. (b) The ratio of the two harmonics is plotted with the corresponding statistical errors.

Bibliography

[1]

[2] Event reconstruction in the {PHENIX} central arm spectrometers. Nucl.Instrum.Meth, A482:491–512, 2002.

[3] Rhic operations with asymmetric collisions in 2015. 2015.

[4] A. et al Adare. Measurements of elliptic and triangular flow in high-multiplicity ${}^{3}\mathrm{He} + \mathrm{Au}$ collisions at $\sqrt{s_{NN}} = 200$ GeV. Phys. Rev. Lett., 115:142301, Sep 2015.

[5] S. S. et al Adler. Absence of suppression in particle production at large transverse momentum in $\sqrt{s_{NN}} = 200$ GeV $d + \mathrm{Au}$ collisions. Phys. Rev. Lett., 91:072303, Aug 2003.

[6] J. et al Beringer. Review of particle physics. Phys. Rev. D, 86:010001, Jul 2012.

[7] Siegfried Bethke. The 2009 world average of α. The European Physical Journal C, 64(4):689–703, 2009.

[8] Fred Cooper and Graham Frye. Single-particle distribution in the hydrodynamic and statistical thermodynamic models of multiparticle production. Phys. Rev. D, 10:186–189, Jul 1974.

[9] S. Eremin and S. Voloshin. Nucleon participants or quark participants? Phys. Rev. C, 67:064905, Jun 2003.

[10] C. Aidala et al. The {PHENIX} forward silicon vertex detector. Nuclear Instruments and Methods in Physics Research Section A: Accelerators, Spectrometers, Detectors and Associated Equipment, 755:44 – 61, 2014.

[11] K. Adcox et al. {PHENIX} detector overview. Nuclear Instruments and Methods in Physics Research Section A: Accelerators, Spectrometers, Detectors and Associated Equipment, 499(2?3):469 – 479, 2003. The Relativistic Heavy Ion Collider Project: {RHIC} and its Detectors.

[12] A Fedotov. Progress of high-energy electron cooling for rhic.

[13] Enrico Fermi. High energy nuclear events. Progress of Theoretical Physics, 5(4):570–583, 1950.

[14] Charles Gale, Sangyong Jeon, Björn Schenke, Prithwish Tribedy, and Raju Venugopalan. Event-by-event anisotropic flow in heavy-ion collisions from combined yang-mills and viscous fluid dynamics. Phys. Rev. Lett., 110:012302, Jan 2013.

[15] M. Habich, J. L. Nagle, and P. Romatschke. Particle spectra and hbt radii for simulated central nuclear collisions of .

[16] M. Habich, J. L. Nagle, and P. Romatschke. Particle spectra and hbt radii for simulated central nuclear collisions of c+c, al+al, cu+cu, au+au, and pb+pb from sqrt(s)=62.4-2760 gev. The European Physical Journal C, 75(1):15, 2015.

[17] Tetsufumi Hirano, Ulrich Heinz, Dmitri Kharzeev, Roy Lacey, and Yasushi Nara. Mass ordering of differential elliptic flow and its violation for ϕ mesons. Phys. Rev. C, 77:044909, Apr 2008.

[18] V. Khachatryan and et al. Evidence for collectivity in pp collisions at the {LHC}. Physics Letters B, 765:193 – 220, 2017.

[19] V. Khachatryan and etal. Observation of long-range, near-side angular correlations in proton-proton collisions at the lhc. Journal of High Energy Physics, 2010(9):91, 2010.

[20] Zi-Wei Lin, Che Ming Ko, Bao-An Li, Bin Zhang, and Subrata Pal. Multiphase transport model for relativistic heavy ion collisions. Phys. Rev. C, 72:064901, Dec 2005.

[21] Guo-Liang Ma and Zi-Wei Lin. Predictions for $\sqrt{s_{NN}} = 5.02$ tev pb + pb collisions from a multiphase transport model. Phys. Rev. C, 93:054911, May 2016.

[22] Stephen J. Sanders Michael L. Miller, Klaus Reygers and Peter Steinberg. Glauber modeling in high-energy nuclear collisions. Annual Review of Nuclear and Particle Science, 57:205–243, 2007.

[23] J. L. Nagle, A. Adare, S. Beckman, T. Koblesky, J. Orjuela Koop, D. McGlinchey, P. Romatschke, J. Carlson, J. E. Lynn, and M. McCumber. Exploiting intrinsic triangular geometry in relativistic $^{3}\mathrm{He} + \mathrm{Au}$ collisions to disentangle medium properties. Phys. Rev. Lett., 113:112301, Sep 2014.

[24] J. D. Orjuela Koop, A. Adare, D. McGlinchey, and J. L. Nagle. Azimuthal anisotropy relative to the participant plane from a multiphase transport model in central $p + \mathrm{Au}$, $d + \mathrm{Au}$, and $^{3}\mathrm{He} +$ Au collisions at $\sqrt{s_{NN}} = 200$ gev. Phys. Rev. C, 92:054903, Nov 2015.

[25] A. M. Poskanzer and S. A. Voloshin. Methods for analyzing anisotropic flow in relativistic nuclear collisions. Phys. Rev. C, 58:1671–1678, Sep 1998.

[26] Johann Rafelski. Connecting qgp-heavy ion physics to the early universe. Nuclear Physics B - Proceedings Supplements, 243:155 – 162, 2013.

[27] P. Romatschke. Light-heavy-ion collisions: a window into pre-equilibrium qcd dynamics? The European Physical Journal C, 75(7):305, 2015.

[28] T. Roser. Rhic performance. Nuclear Physics A, 698(1):23 – 28, 2002.

[29] Björn Schenke, Prithwish Tribedy, and Raju Venugopalan. Fluctuating glasma initial conditions and flow in heavy ion collisions. Phys. Rev. Lett., 108:252301, Jun 2012.

[30] Bjrn Schenke and Raju Venugopalan. Collective effects in lightheavy ion collisions. Nuclear Physics A, 931:1039 – 1044, 2014. {QUARK} {MATTER} 2014XXIV {INTERNATIONAL} {CONFERENCE} {ON} {ULTRARELATIVISTIC} NUCLEUS-NUCLEUS {COLLISIONS}.

[31] Sren Schlichting and Bjrn Schenke. The shape of the proton at high energies. Physics Letters B, 739:313 – 319, 2014.

[32] Huichao Song. Hydrodynamic modelling for relativistic heavy-ion collisions at rhic and lhc. Pramana, 84(5):703–715, 2015.

[33] Wilke van der Schee, Paul Romatschke, and Scott Pratt. Fully dynamical simulation of central nuclear collisions. Phys. Rev. Lett., 111:222302, Nov 2013.

[34] Kevin Welsh, Jordan Singer, and Ulrich Heinz. Initial-state fluctuations in collisions between light and heavy ions. Phys. Rev. C, 94:024919, Aug 2016.

[35] XIAO-MING XU. ORIGIN OF TEMPERATURE OF QUARK-GLUON PLASMA IN HEAVY ION COLLISIONS, pages 203–208. WORLD SCIENTIFIC, 2015.